# This article is licensed under a Creative Commons Attribution-NonCommercial 3.0 Unported Licence.

# Journal of Materials Chemistry A



**View Article Online PAPER** View Journal



Cite this: DOI: 10.1039/d5ta06486d

# Come for predictions, stay for complexity: synthesis and experimental probing of ionic conductivity in Li<sub>9</sub>B<sub>19</sub>S<sub>33</sub>

Richeal A. Oppong, ab Scott A. Southern, Chris Martin, Isabella Freebairn, Arka Sarkar, Dad Yao Abusa, Gayatri Viswanathan, Dad Frédéric A. Perras, Dac 

Lithium thioborates, despite their potential cost-effectiveness and low density, have received considerably less attention as solid electrolytes compared to their thiophosphate counterparts. A primary obstacle to their widespread investigation has been the inherent challenge in synthesizing single-phase materials. Computational studies have predicted several lithium thioborate phases exhibiting high ionic conductivity, with Li<sub>9</sub>B<sub>19</sub>S<sub>33</sub> notably predicted to reach 80 mS cm<sup>-1</sup>. However, experimental validation of these theoretical predictions remains absent. This work addresses this gap by detailing a successful synthesis of the previously elusive Li<sub>9</sub>B<sub>19</sub>S<sub>33</sub> phase, facilitated by in situ temperature dependent powder X-ray diffraction. Our findings reveal the peritectic nature of phase formation, necessitating an excess of boron sulfide in the reaction mixture. We further present a comprehensive structural characterization of Li<sub>9</sub>B<sub>19</sub>S<sub>33</sub> utilizing spectroscopic techniques like NMR, FT-IR, and diffuse reflectance and report on its ionic conductivity. Solid-state <sup>6</sup>Li NMR line narrowing experiments revealed an ion mobility activation energy of 0.26 eV whereas activation energies derived from impedance spectroscopy measurements were significantly higher, resulting in lower than theoretically predicted ionic conductivity.

Received 11th August 2025 Accepted 11th November 2025

DOI: 10.1039/d5ta06486d

rsc.li/materials-a

# Introduction

Central to the functionality of electric vehicles (EVs) are their batteries. Currently, the most widely used lithium-ion batteries utilize organic liquid electrolytes (OLEs), that involve inherent risks owing to their flammability and the potential for spontaneous combustion. To address this issue and achieve higher energy densities, all-solid-state batteries (ASSBs) are being developed. Solid electrolytes (SEs) are the critical component of ASSBs and can be made from materials such as sulfides, oxides, polymers, halides, or hydrides.<sup>2-10</sup> For a solid electrolyte to be high performing, it must exhibit high ionic conductivity, low electrical conductivity, and a wide electrochemical stability window.11,12

The high polarizability of S<sup>2-</sup> ions tends to facilitate the mobility of Li<sup>+</sup> ions. 13,14 Additionally, sulfur's large ionic radius can create bigger conduction channels and/or larger accessible empty volumes for Li<sup>+</sup> ion diffusion enabling sulfide SEs to have (typically) significantly higher ionic conductivities than a corresponding oxide SE. In particular, lithium thiophosphate-based SEs have shown promise in this field owing to their high ionic conductivity, mechanical ductility, and low mass density. 15-18 Some noteworthy examples are  $\text{Li}_{10}\text{GeP}_2\text{S}_{12}$  and  $\text{Li}_{9.54}\text{Si}_{1.74}\text{P}_{1.44}\text{S}_{11.7}\text{Cl}_{0.3}$  that have room temperature ionic conductivities of 12 mS cm<sup>-1</sup> and 25 mS cm<sup>-1</sup>, respectively.<sup>9,19</sup> These conductivities are comparable to, or even surpass, traditional OLEs. However, these thiophosphates have a narrow electrochemical stability window<sup>20</sup> which limits their stability in contact with low voltage Li metal anodes and high voltage transition metal cathodes. Additionally, the use of germanium in Li<sub>10</sub>GeP<sub>2</sub>S<sub>12</sub> makes it costly, emphasizing the need for more affordable sulfide electrolyte alternatives.

Utilizing Density Functional Theory (DFT) calculations coupled with grand potential phase analysis, four single-crystal phases of lithium thioborate, Li<sub>3</sub>BS<sub>3</sub>, Li<sub>2</sub>B<sub>2</sub>S<sub>5</sub>, Li<sub>5</sub>B<sub>7</sub>S<sub>13</sub>, and Li<sub>9</sub>B<sub>19</sub>S<sub>33</sub> have been predicted to exhibit high ionic conductivity and a wider electrochemical stability window.21 Despite these theoretical findings, the experimental realization of phase-pure material for any of these phases has proven difficult, often resulting in multiphase mixtures. This is because lithium thioborates generally require higher temperatures and longer annealing times when compared with thiophosphates. Syntheses of thioborates is typically done inside sealed silica glass ampoules which are known to react vigorously with B2S3 at

<sup>&</sup>lt;sup>a</sup>Department of Chemistry, Iowa State University, Ames, Iowa 50011, USA. E-mail: kovnir@iastate.edu

<sup>&</sup>lt;sup>b</sup>Department of Materials Science and Engineering, Iowa State University, Ames, Iowa 50011. USA. E-mail: swmartin@iastate.edu

Chemical and Biological Sciences Division, Ames National Laboratory, Ames, Iowa 50011, USA

<sup>&</sup>lt;sup>d</sup>Materials Sciences and Engineering Division, Ames National Laboratory, Ames, Iowa 50011. USA

temperatures above 450 °C.<sup>22,23</sup> For these reasons, it has been challenging to obtain a single phase of thioborates materials.

Kaup *et al.* reported the synthesis of  $\text{Li}_{6+2x}[B_{10}S_{18}]S_x$  (x=2) with substantial  $\text{Li}_5B_7S_{13}$  and  $\text{Li}_3BS_3$  impurities. Fimilarly, attempts to make  $\text{Li}_5B_7S_{13}$ , resulted in a multiphase mixture of  $\text{Li}_{6+2x}[B_{10}S_{18}]S_x$  and  $\text{Li}_9B_{19}S_{33}$ . A more recent study of the lithium thioborate  $\text{Li}_{6+2x}[B_{10}S_{18}]S_x$  (x=1) showed that nonstoichiometric nominal compositions with excess of B and/or S were needed for the formation of the target phase while stoichiometric nominal compositions resulted in a mixture of undesired ternary phases. Out of the four computationally predicted phases with high conductivity,  $\text{Li}_9B_{19}S_{33}$  is expected to exhibit an impressive ionic conductivity of 80 mS cm<sup>-1</sup> at 25 °C. Experimental evidence to confirm this finding has yet to be obtained. Although the crystal structure of this phase was reported three decades ago, the syntheses of single phase samples to characterize properties remain elusive.

In this work, we describe strategies to counter the challenges encountered during the synthesis of  $\text{Li}_9\text{B}_{19}\text{S}_{33}$ . We concluded that the  $\text{Li}_9\text{B}_{19}\text{S}_{33}$  behaves as a peritectic compound, requiring an excess of  $\text{B}_2\text{S}_3$  to inhibit the formation of secondary phases such as  $\text{Li}_{6+2x}[\text{B}_{10}\text{S}_{18}]\text{S}_x$ . Hereafter, the  $\text{Li}_{6+2x}[\text{B}_{10}\text{S}_{18}]\text{S}_x$  phases, where x=1 or 2, will be referred to simply as LiBS2. The influence of varying the amount of boron sulfide on the material's ionic conductivity was also explored. These results may inform the way for further investigations into obtaining this and other LBS phases in phase pure form and characterization of their properties.

# Results and discussion

### **Synthesis**

A high-temperature solid state approach was used to synthesize  $\text{Li}_9\text{B}_{19}\text{S}_{33}$ . In an Ar-filled glove box (<1 ppm  $\text{O}_2$  and  $\text{H}_2\text{O}$ ), appropriate amounts of starting materials, either  $\text{Li}_2\text{S} + \text{B} + \text{S}$  or

Li<sub>2</sub>S + B<sub>2</sub>S<sub>3</sub>, were ground using an agate mortar and pestle to ensure a homogenous mixture. This mixture was then transferred into a carbon-coated silica ampoule. The ampoule was evacuated, sealed using a hydrogen/oxygen torch, heated to 750 °C over a period of 4 h, and held for 2 h. It was then cooled to 550 °C and held for 4 h before being slowly cooled to room temperature over a period of 12 h. Once cooled, the ampoule was opened in the glovebox. The final product was gently separated to find crystals suitable for single crystal X-ray diffraction. The remaining crystals, and those from subsequent synthesis preparations, were crushed into a polycrystalline powder for powder X-ray diffraction (PXRD), Fourier transform infrared (FT-IR) spectroscopy, nuclear magnetic resonance (NMR) spectroscopy, UV-Vis spectroscopy, and Li<sup>+</sup> ionic conductivity measurements.

Initial experiments targeting the Li<sub>9</sub>B<sub>19</sub>S<sub>33</sub> phase from stoichiometric nominal compositions resulted in multiphase mixtures containing LiBS2 as major phase and Li5B7S13 as a small admixture (Table S1). Using different reaction containers such as carbonized silica ampoules, BN crucibles, or vitreous carbon crucibles, did not change the reaction outcomes, yet some reactions of presumably B<sub>2</sub>S<sub>3</sub> with container or ampoule walls was observed in all cases. To overcome diffusion limitations at lower synthetic temperatures, ball-milling the reactants and pressing a pellet were attempted. Annealings of such samples at 400 °C resulted in no visible reaction with container, however, such low temperature annealings led to the formation of only lithiumrich thioborate phase, Li<sub>3</sub>BS<sub>3</sub> (Fig. S7). To better understand the complex synthetic process, an in situ PXRD experiment was conducted at beamline 17-BM at the Advanced Photon Source at Argonne National Laboratory (Fig. 1A and B). From room temperature to approximately 200 °C only a single crystalline phase, Li2S, was observed. Due to the amorphous nature of  $B_2S_3$ , it was undetectable by PXRD. As temperature increases,

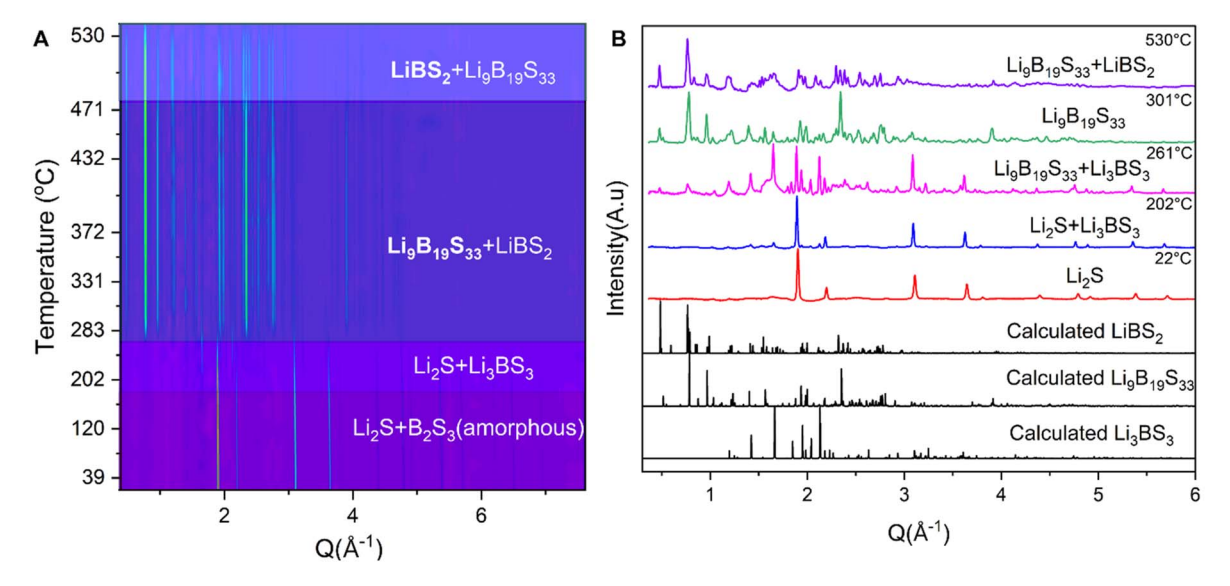


Fig. 1 (A) In situ powder X-ray diffraction studies on the synthesis of the target phase  $\text{Li}_9\text{B}_{19}\text{S}_{33}$  showing the concurrent formation of LiBS<sub>2</sub> over a wide temperature range. (B) Selected powder patterns from in situ studies compared to calculated patterns ( $\lambda = 0.2411 \text{ Å}$ ).

a reaction between Li<sub>2</sub>S and B<sub>2</sub>S<sub>3</sub> led to the formation of Li<sub>3</sub>BS<sub>3</sub>, which is the phase with the lowest B<sub>2</sub>S<sub>3</sub> content among the known LBS phases. The LiBS2 phase forms in tandem with the target phase, Li<sub>9</sub>B<sub>19</sub>S<sub>33</sub>, at temperatures as low as 285 °C and those two phases coexist over a wide range of temperatures. At lower temperatures (or shorter reaction times; this was a constant heating rate experiment), Li<sub>9</sub>B<sub>19</sub>S<sub>33</sub> was predominant; but, with increasing time and temperature, equilibrium shifts to LiBS2 as the major phase.

The discrepancy between in situ and ex situ findings, particularly regarding the formation of the target phase, may be attributed to variations in temperature reading accuracy, the reduced diffusion limitations due to small sample size, and, notably, the heating rates used. In situ experiments were conducted with a sample size of  $\sim$ 20 mg and a heating rate of 20  $^{\circ}$ C min $^{-1}$ , while ex situ sample size was significantly larger, 300-500 mg, with a much slower heating rate of approximately 3  $^{\circ}$  $C \min^{-1}$ .

From the in situ PXRD experiments, we realized that obtaining phase-pure Li<sub>9</sub>B<sub>19</sub>S<sub>33</sub> from stoichiometric amounts of the reactants would be challenging, as the more thermodynamically stable phase (LiBS2) is likely to form in line with observations in previous studies.25 It was hypothesized that the Li<sub>9</sub>B<sub>19</sub>S<sub>33</sub> phase is a peritectic phase, thus required excess amounts of B<sub>2</sub>S<sub>3</sub> for the reaction to proceed (Fig. S4). A similar scenario was recently reported, where excess B<sub>2</sub>S<sub>3</sub> was needed to synthesize LiBS<sub>2</sub> and minimize formation of admixtures.<sup>26</sup>

In Fig. 2A, selected PXRD patterns show that the Li<sub>9</sub>B<sub>19</sub>S<sub>33</sub> phase formed with no crystalline admixtures when 6 to 15 molar equivalent excess B<sub>2</sub>S<sub>3</sub> were used during the synthesis. Below this range, the formation of Li<sub>9</sub>B<sub>19</sub>S<sub>33</sub> phase is challenging. Rietveld refinement of high-resolution room temperature synchrotron PXRD data (Fig. 2B) confirmed the absence of secondary crystalline phases such as Li2S, LiBS2, Li3BS3, or

Li<sub>5</sub>B<sub>7</sub>S<sub>13</sub>, demonstrating the purity of our sample. The hump observed from 1  $\text{Å}^{-1}$  to 2.5  $\text{Å}^{-1}$  in Fig. 2B is as a result of some leftover B<sub>2</sub>S<sub>3</sub> because this sample was prepared with excess 15 molar equivalents of B2S3 with respect to Li9B19S33 and some background due to silica capillary. The refinement was done using a crystal structure model derived from single crystal X-ray diffraction studies. The diffraction pattern obtained was indexed to a monoclinic unit cell with parameters a = 23.618(3)Å, b = 14.355(8) Å, c = 12.239(8) Å, and  $\beta = 103.79(4)$  Å. There are no unaccountable peaks, and the lattice parameters are close to the initially reported crystal structure by Krebs et al. 23 In this way, a reasonable agreement between the experimental and calculated patterns was achieved.

### Crystal structure

Single crystal X-ray diffraction (SCXRD) findings align with an initial report<sup>23</sup> that Li<sub>9</sub>B<sub>19</sub>S<sub>33</sub> crystallizes in the C2/c space group; however, we observed a lower unit cell volume due to differences in the experiment temperatures (173 K vs. 298 K). The crystal structure of Li<sub>9</sub>B<sub>19</sub>S<sub>33</sub> consists of boron tetrahedrally coordinated to sulfur, forming a super tetrahedral structure made up of corner-sharing B<sub>10</sub>S<sub>20</sub> units (Fig. 3B and C). Lithium atoms are distributed over 7 Li sites located in the framework channels. The main disparity between the structure determined here and previously reported crystal structures lies in the differences in Li occupancies, as shown in Table S2. There is an additional disorder in the Li sublattices, such as the split Li site labelled Li4 and Li44 which have 73% and 27% occupancies, respectively, (Fig. S3). Lithium atoms have different coordination environment in this structure. Li1, Li2, Li3, Li4, Li5, and Li6 have distorted octahedral coordination by 6 S atoms, whereas Li44 and Li7 are tetrahedrally coordinated by 4 S atoms. The majority of Li@S<sub>r</sub> polyhedra are interconnected

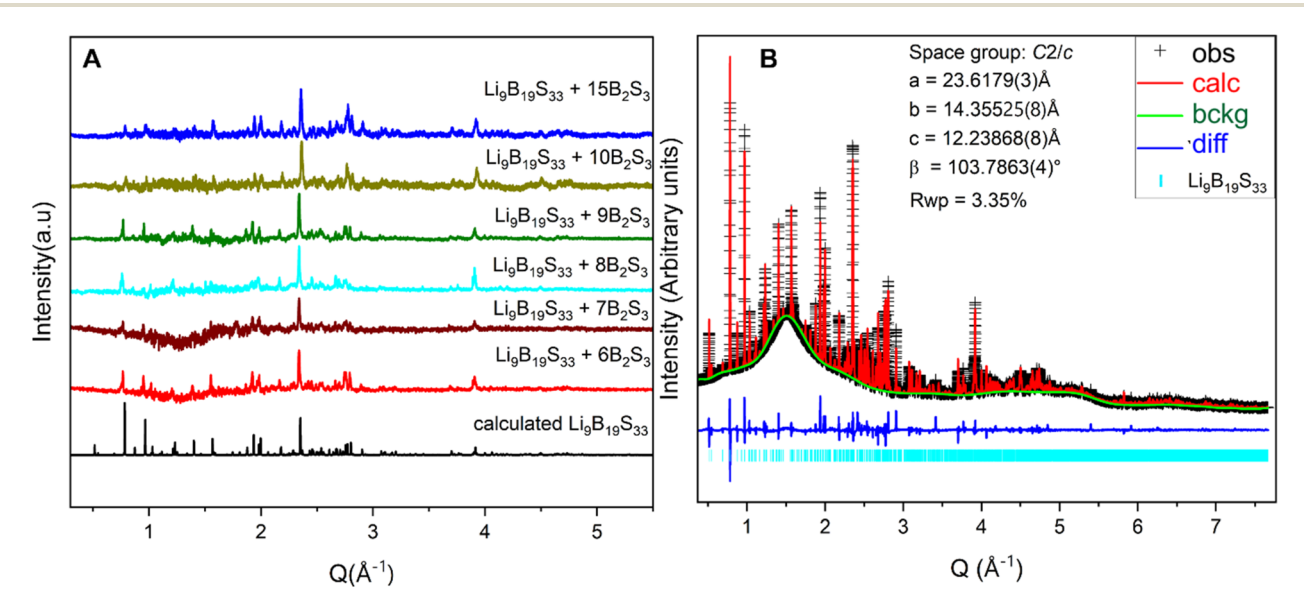


Fig. 2 (A) PXRD patterns of  $\text{Li}_9\text{B}_{19}\text{S}_{33}$  when different excess amounts of  $\text{B}_2\text{S}_3$  were used for synthesis. The negative background around 1.1 Å $^{-1}$  to  $1.8~\text{Å}^{-1}$  is a result of subtraction from blank holders. (B) Rietveld refinement of high-resolution data with wavelength  $\lambda=0.8613~\text{Å}$ . The data were refined against the structural model from SCXRD.

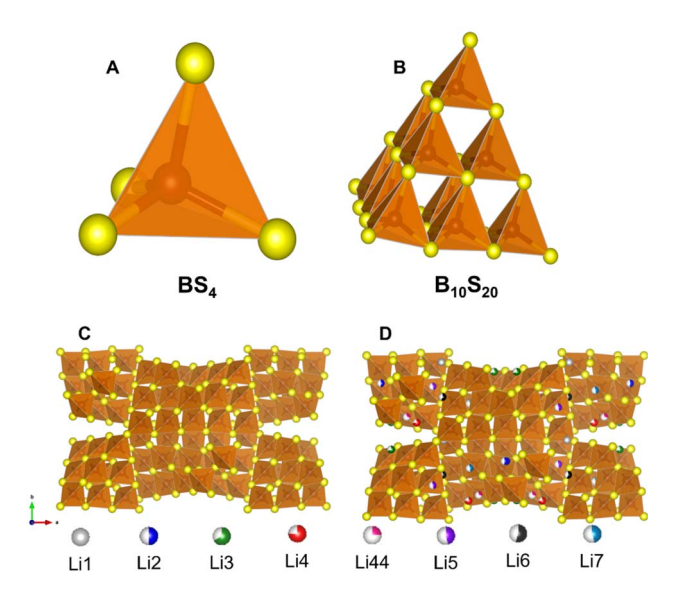


Fig. 3 Crystal structure of  $\text{Li}_9\text{B}_{19}\text{S}_{33}$ . (A) Tetrahedrally coordinated boron. (B)  $\text{B}_{10}\text{S}_{20}$  super tetrahedron formed from corner sharing BS<sub>4</sub> tetrahedra. (C) B–S framework of  $\text{Li}_9\text{B}_{19}\text{S}_{33}$ . (D) Crystal structure of  $\text{Li}_9\text{B}_{19}\text{S}_{33}$  with partially occupied Li ions sites.

through corner sharing. Additionally, polyhedra around Li2, Li44, and Li7 are linked *via* edge-sharing connections (Fig. S6).

### NMR and FT-IR spectroscopy

Given that an excess of  $B_2S_3$  is required to drive the formation of the target phase, it is important to account for the unreacted  $B_2S_3$  remaining after synthesis, as it is not fully incorporated into the final product. Interestingly, it is observed that  $B_2S_3$  tends to segregate on the outer surface of the reaction ingot,

where it reacts with the silica ampoule (Fig. S10 and S11). To further investigate this behavior, we examine the coordination environments in both the target  $\text{Li}_9B_{19}S_{33}$  compound and  $B_2S_3$ . In the target compound, B is coordinated in a tetrahedral geometry by sulfur atoms, whereas in  $B_2S_3$ , boron adopts a trigonal-planar coordination environment. This distinction suggested the use of Fourier-transform infrared (FT-IR) spectroscopy to examine the relative amounts of tetrahedral to trigonal boron in the synthesized sample.

The sample used for this study was one synthesized with the excess amount of B<sub>2</sub>S<sub>3</sub> (8 molar equivalents). The FT-IR spectrum of B<sub>2</sub>S<sub>3</sub> (Fig. 4B) reveals broad intense vibrational modes characteristic of trigonal boron environments due to its amorphous nature. Specifically, modes near >750 cm<sup>-1</sup> correspond to isolated BS<sub>3</sub> short-range order (SRO) units, while a distinct band at  $\sim 1000 \text{ cm}^{-1}$  is attributed to trigonal boron sites within hexagonal B<sub>3</sub>S<sub>3</sub> ring structures. Notably, vibrational modes associated with tetrahedrally coordinated boron (BS4 units), which are typically expected below 700 cm<sup>-1</sup>, are absent. In contrast, the spectrum of the target compound, Li<sub>9</sub>B<sub>19</sub>S<sub>33</sub> (Fig. 4A), exhibits prominent features associated with tetrahedral boron, manifested as a strong doublet centered at  $\sim$ 640 cm<sup>-1</sup>,  $\sim$ 667 cm<sup>-1</sup> and the signal  $\sim$ 750 cm<sup>-1</sup>. Peaks corresponding to trigonal boron environments are significantly less intense, indicating a dominant tetrahedral coordination in the final product. These assignments are based on the work of Cho et al., who investigated the FT-IR spectra of lithium thioborate polycrystals and glasses, including LiBS2 and identified IR modes of BS<sub>4</sub> in 750-600 cm<sup>-1</sup> range. Both Li<sub>9</sub>B<sub>19</sub>S<sub>33</sub> and LiBS<sub>2</sub> predominantly contain tetrahedrally coordinated boron SRO units, leading to similar FT-IR spectral features.27 Similar spectroscopic results were also observed for silver thioborate phases, further supporting the assignments above.28

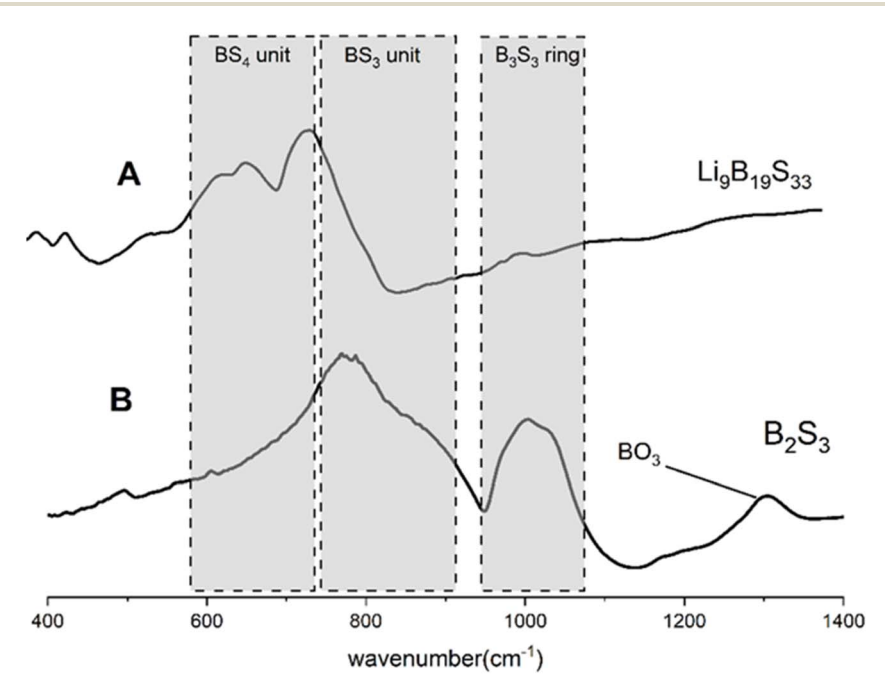


Fig. 4 FT-IR spectra of (A)  $\text{Li}_9\text{B}_{19}\text{S}_{33}$  and (B)  $\text{B}_2\text{S}_3$  samples depicting mostly  $\text{BS}_4$  modes in  $\text{Li}_9\text{B}_{19}\text{S}_{33}$  and intense  $\text{BS}_3$  in the boron sulfide sample.

<sup>11</sup>B magic-angle spinning (MAS) solid-state NMR spectra were collected for both Li<sub>9</sub>B<sub>19</sub>S<sub>33</sub> and B<sub>2</sub>S<sub>3</sub> (used as a reference) at room temperature, Fig. 5. The <sup>11</sup>B spectrum of B<sub>2</sub>S<sub>3</sub>, Fig. 5B, is dominated by a broad signal from 45 to 65 ppm, corresponding to boron atoms in trigonal planar environments, with minor peaks corresponding to B2SO and BSO2 SRO units which were also observed in the FT-IR spectra ~1200 cm<sup>-1</sup>.<sup>29-32</sup> Conversely, the spectrum of the Li<sub>9</sub>B<sub>19</sub>S<sub>33</sub>, Fig. 5A, predominantly features a resonance close to 0 ppm corresponding to tetrahedral BS<sub>4</sub> SRO units, alongside minor signals indicative of BS3, B2SO, BSO2, and BO3 SRO units, presumably located at particle surfaces.

The BS<sub>4</sub> region in the <sup>11</sup>B multiple-quantum magic-angle spinning (MQMAS) NMR spectrum (Fig. 5C) suggests the presence of two sites, similar to what was observed for a Na<sub>3</sub>B<sub>5</sub>S<sub>9</sub> solid electrolyte.33 There, two BS<sub>4</sub> fractions were identified with a 4:6 ratio, corresponding to corner and edge tetrahedral BS<sub>4</sub> species. The corner sites appear to be quite homogeneous while the edge sites appear to be broadened by a distribution of chemical shifts. Our NMR observations for tetrahedral B in Li<sub>9</sub>B<sub>19</sub>S<sub>33</sub> (Fig. 5C) are similar to what was observed for the Na<sub>3</sub>B<sub>5</sub>S<sub>9</sub> system, suggesting a difference between the edge and corner sites in the association of lithium ions.33 Notably, the intensity ratio of the BS4 to BS3 peaks in both FT-IR and NMR spectra is approximately 80:20, indicating that despite the use of substantial molar equivalents of B<sub>2</sub>S<sub>3</sub> in addition to the stoichiometric amount required for Li<sub>9</sub>B<sub>19</sub>S<sub>33</sub> synthesis, only a minimal amount of B<sub>2</sub>S<sub>3</sub> remained in the target sample after synthesis.

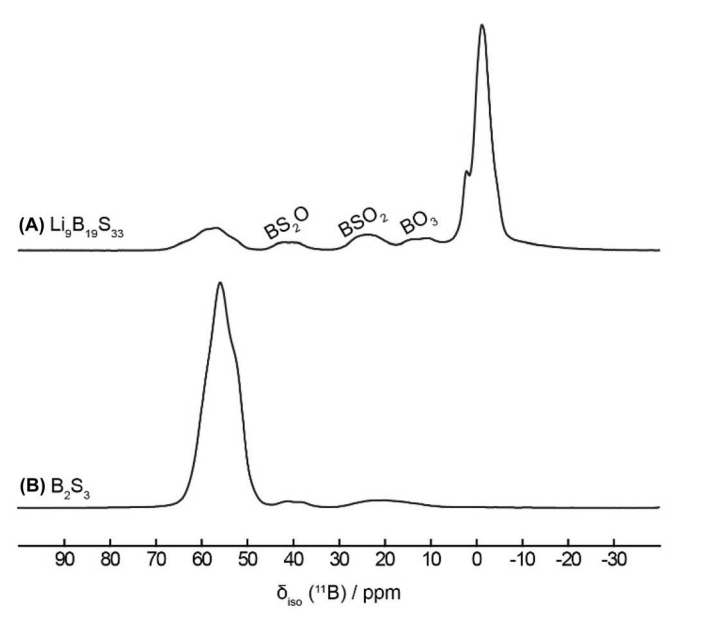
To determine the threshold of excess boron sulfide needed to obtain a single phase Li<sub>9</sub>B<sub>19</sub>S<sub>33</sub> from PXRD, we varied the amounts of B<sub>2</sub>S<sub>3</sub>, ranging from 1 to 10 molar equivalents. It was observed that using <6 molar equivalents of B2S3 resulted in amorphous phases or LiBS2. Use of 6-10 molar equivalents, however, resulted in the formation of Li<sub>9</sub>B<sub>19</sub>S<sub>33</sub>. <sup>11</sup>B NMR spectroscopy was used to determine the ratio of trigonal boron to tetrahedral boron in samples with 8, 9, and 10 mole equivalents of B<sub>2</sub>S<sub>3</sub> (Fig. S1 and S2). A consistent decrease in the intensity of trigonal boron signal was observed when compared with nominal composition. In the sample with 8 mole equivalents of B<sub>2</sub>S<sub>3</sub>, the ratio of tetrahedral to trigonal boron was 85: 15, indicating the losses of B<sub>2</sub>S<sub>3</sub> during reaction, presumably due to reaction with the silica ampoule.

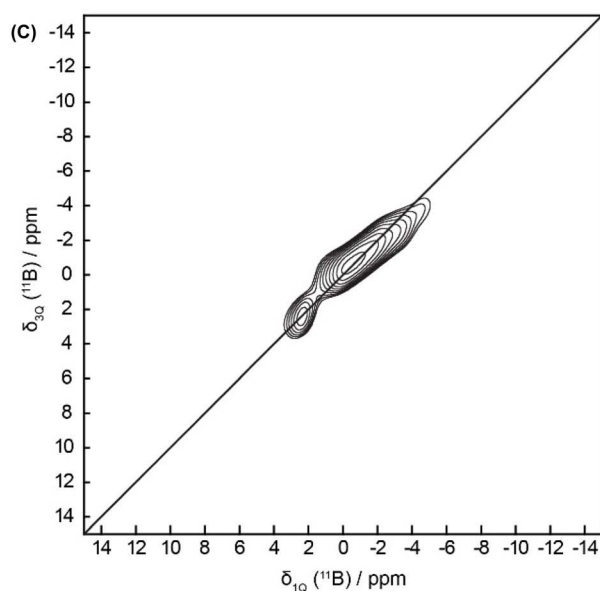
## <sup>6</sup>Li motional line narrowing experiment

NMR spectroscopy has been widely employed to investigate microscopic lithium-ion mobility. One common approach is the Waugh-Fedin model<sup>34</sup> which enables the estimation of the activation energy  $(E_{\Delta})$  from the motional narrowing of the static <sup>6</sup>Li NMR line shape. Variable temperature <sup>6</sup>Li static NMR experiments were acquired for this purpose (Fig. 6A). The sample used in this experiment was synthesized with 15 molar equivalents of excess boron sulfide. Residual B<sub>2</sub>S<sub>3</sub> present after synthesis does not affect the intrinsic properties of the Li line narrowing, allowing for an accurate assessment of the material's activation energy. The spectral line shapes exhibited a transition from Gaussian to Lorentzian profiles, indicating changes in the Li-ion dynamics. With increasing temperature, the onset of ionic motion led to the temporal averaging of anisotropic interactions. Line narrowing was first observed around 167 K and progressed until 220 K, beyond which no further narrowing occurred. Using the Waugh-Fedin model, 35,36 the line width at half height was plotted as a function of temperature, and the extrapolated onset temperature  $(T_{onset})$ was determined to be 162 K (Fig. 6B). The activation energy was calculated to be  $0.26 \text{ eV mol}^{-1}$  using the following relationship:

$$E_{\rm A} = 1.617 \times 10^{-3} \,\text{eV K}^{-1} \times T_{\text{onset}}$$
 (1)

This measurement is in agreement with the value of 0.23 eV measured by Krebs et al.37





 $^{11}$ B MAS NMR spectra of (A) Li $_9$ B $_{19}$ S $_{33}$  and (B) B $_2$ S $_3$  samples. (C) 2D MQMAS showing the two tetrahedral boron sites in Li $_9$ B $_{19}$ S $_{33}$ .

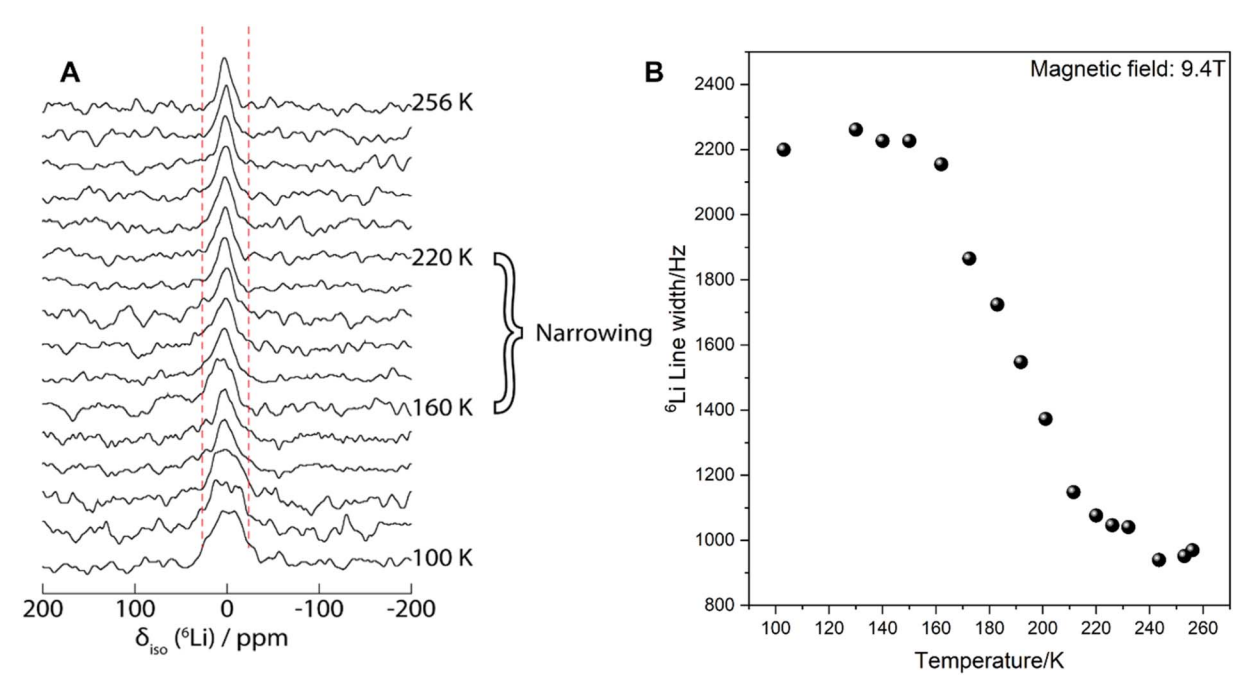


Fig. 6 (A) Variable-temperature  $^6$ Li static line width measurements for Li<sub>9</sub>B<sub>19</sub>S<sub>33</sub>. (B)  $^6$ Li NMR peak width at half height as a function of temperature, highlighting the onset temperature at which linewidth narrowing occurs.

### **UV-Vis spectroscopy**

SEs require wide bandgaps which serve to inhibit parasitic electronic conductivity and widen the electrochemical stability window. A study conducted by Muy et al. utilizing highthroughput screening of various SEs demonstrated that an increase in band gap correlates with a broader electrochemical stability window.38 This finding highlights the necessity of selecting materials with large bandgap energies for SEs. Further investigations, including those based on DFT calculations, identified several sulfide-based SEs with bandgaps exceeding 4 eV. Notable examples include lithium thioborate such as Li<sub>3</sub>BS<sub>3</sub> and Li<sub>2</sub>B<sub>2</sub>S<sub>5</sub>, both of which exhibit bandgaps greater than 4 eV.39 The large bandgaps of these materials are significant as they categorize them as electronic insulators, a crucial feature of SEs, where insulating properties help prevent unwanted electron conduction. Sendek et al. employed DFT calculations to predict the electronic band gap of Li<sub>9</sub>B<sub>19</sub>S<sub>33</sub>. Their calculations estimated the bandgap to be 2.9 eV and 4.0 eV using the PBE and HSE06 exchange-correlation functionals, respectively.21 While the specific nature of the energy bandgap (direct or indirect) was not explicitly stated in their work, our diffuse reflectance measured provide further insight. Direct and indirect bandgaps of 3.26(4) eV and 3.00(4) eV, respectively, were observed for Li<sub>9</sub>B<sub>19</sub>S<sub>33</sub> (Fig S5). These experimental results are consistent with the optical properties of the material, as evidenced by its nearly transparent, colorless crystals and the pale gray hue of powdered samples. This correspondence between calculated and experimentally observed bandgaps reinforces the material's potential for use in electrochemical applications requiring high electrochemical stability and low electrical conductivity.

### Electrochemical impedance spectroscopy

The ionic conductivity of Li<sub>9</sub>B<sub>19</sub>S<sub>33</sub> was measured using a Novocontrol Concept 80 dielectric spectrometer. We conducted isothermal frequency scans ranging from 0.1 Hz to 7 MHz. By comparing pellets of different densities, the impact of fabrication conditions on ionic conductivity was investigated. Our findings indicated that an increase in fabrication pressure results in a linear increase in pellet density. According to Diallo et al., a relative density of approximately 95% is necessary to close any percolating pore network, which can affect the measurement of ionic conductivity.40 In agreement with that hypothesis, a pellet of Li<sub>9</sub>B<sub>19</sub>S<sub>33</sub> with a density of around 54.5% exhibited two orders of magnitude lower ionic conductivity than that of a Li<sub>9</sub>B<sub>19</sub>S<sub>33</sub> pellet with 95% density (Fig. 7A). Additionally, samples were prepared and measured with varying amounts of excess B2S3 (Fig. 7B). There was no significant difference in the room temperature conductivities of these samples; the conductivity at room temperature of the sample prepared with 6 molar equivalents of B<sub>2</sub>S<sub>3</sub> was 0.058 mS cm<sup>-1</sup>, while that of the sample prepared with 8 molar equivalents was  $0.052 \text{ mS cm}^{-1}$ .

Typically, sulfide-based solid electrolytes with activation energies in this range of  $\sim$ 0.26 eV tend to exhibit ionic conductivities on the order of or exceeding 1 mS cm $^{-1}$ . The ionic conductivity can be estimated from activation energy Arrhenius relationship

$$\sigma = \sigma_0 \exp(-E_a/k_{\rm B}T) \tag{2}$$

where  $k_{\rm B}$  is the Boltzmann constant. The estimated conductivity will depend on the pre-exponential factor  $(\sigma_0)$  which can be as high as  $\sim 5 \times 10^2$  S cm<sup>-1</sup> for this class of materials.<sup>41</sup> In Fig. 7c

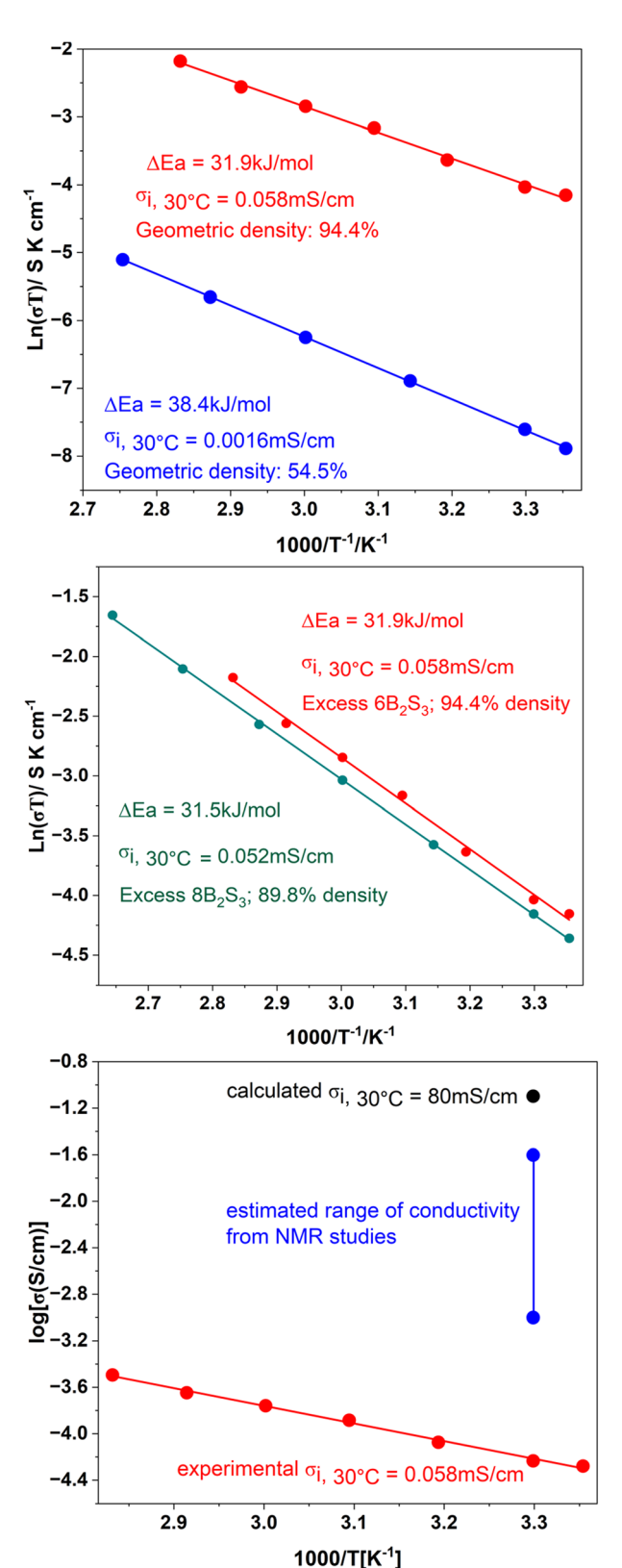


Fig. 7 Arrhenius relationship between ionic conductivity and temperature for (A) Li $_9$ B1 $_9$ S3 $_3$  samples with identical nominal B $_2$ S3 $_3$  excess and with geometric density of 94.4% and 54.4%, and (B) Li $_9$ B1 $_9$ S3 $_3$  prepared with 6 vs. 8 equivalents of B $_2$ S3 $_3$  (C) Comparing conductivity of Li $_9$ B1 $_9$ S3 $_3$  synthesized in this work against the DFT-predicted conductivity reported in Sendek $^{21}$  et al. and the conductivity from NMR linewidth motional narrowing.

a range of the estimated values is shown for different values of the pre-exponential factor. The NMR estimated value agrees with computational predictions but is notably higher than that experimentally measured ionic conductivity. The observed discrepancies are likely due to grain boundary impedances within the pellet, as well as the presence of residual  $B_2S_3$ , which does not affect the NMR linewidth measurements, since NMR selectively probes Li ion dynamics through line narrowing effect.

These discrepancies are not uncommon and are typically associated with the length scales of the different measurements. For instance, pulsed field gradient (PFG) NMR experiments which probe long-range diffusion, have been shown to agree relatively well with EIS for Li7SiPS8.42 Relaxation characteristics and line narrowing, however, are primarily driven by short-range dynamics such as the hopping of a Li ion between two adjacent crystallographic positions. Examples include superionic glasses  $(AgI)_x(Ag_2O \cdot 2B_2O_3)_{1-x}$  (ref. 43) and Li<sub>4-2x</sub>·Mg<sub>x</sub>P<sub>2</sub>S<sub>6</sub>.<sup>36</sup> Additionally, Borsa et al. found that the preexponential factor derived from NMR measurements in Li<sub>2</sub>S-SiS<sub>2</sub> glasses was higher than that obtained from conductivity measurement by an order of magnitude.44 Svare et al. reported that such discrepancies are more pronounced in disordered materials, such as inorganic glasses, than in ordered systems such as that reported here. 45 This behavior is often attributed to the reduced average number of available hopping sites in ordered structures. Additionally, the presence of oxide impurities, as identified by FT-IR and <sup>11</sup>B NMR spectroscopy, may contribute to the observed decrease in ionic conductivity. Such impurities can disrupt the continuous sulfide framework and introduce insulating phases, thereby hindering lithium-ion migration within the structure.46

# Conclusion

Crystalline lithium thioborates, while cost-effective and having low mass density, have been underexplored as SEs. It was predicted that four of these phases are likely to exhibit Li<sup>+</sup> ionic conductivities much higher than 1 mS cm<sup>-1</sup>, with Li<sub>9</sub>B<sub>19</sub>S<sub>33</sub> having the highest anticipated ionic conductivity. Challenges in obtaining a phase-pure product prevented experimental validation. In this study, we successfully synthesized this elusive phase by optimizing the reaction conditions, aided by in situ powder X-ray diffraction studies. We confirmed the formation of this crystalline phase using FT-IR spectroscopy and <sup>11</sup>B NMR techniques. We discovered that the phase is a peritectic phase, requiring excess boron sulfide for its formation, which resulted in residual amorphous boron sulfide in the final product. EIS measurements yielded activation energies ranging from 0.32 eV to 0.40 eV, significantly higher than those measured using 6Li NMR spectroscopy (0.26 eV). Although such discrepancies are not uncommon due to the differing length scales probed by these measurement techniques, the observed variation in ionic conductivity is notably large. This suggests that the material's performance as an ion conductor could be further enhanced through additional synthetic modifications aimed at removing residual boron sulfide.

# **Author contributions**

The manuscript was written through contributions of all authors.

# Conflicts of interest

The authors declare there are no conflicts of interest.

# Data availability

CCDC 2475362 (Li<sub>9</sub>B<sub>19</sub>S<sub>33</sub>) contains the supplementary crystallographic data for this paper. 47

The data supporting this article have been included as part of the supporting information (SI). Supplementary information: description of the synthetic and characterization experimental procedures, as well as additional tables and figures related to diffuse reflectance spectroscopy, crystallographic data, differential scanning calorimetry (DSC) and a schematic phase diagram of Li<sub>9</sub>B<sub>19</sub>S<sub>33</sub>. It also features FT-IR and NMR spectra of Li<sub>9</sub>B<sub>19</sub>S<sub>33</sub> samples synthesized with varying amounts of excess B<sub>2</sub>S<sub>3</sub>, along with a comparison of the unit cells of our synthesized Li<sub>9</sub>B<sub>19</sub>S<sub>33</sub> to those reported in the literature, highlighting the lithium sites and their occupancies. See DOI: https:// doi.org/10.1039/d5ta06486d.

# Acknowledgements

This research was supported by the National Science Foundation ENG/CBET EAGER grant # 2234046. The FTIR spectrometer used in this study was supported by NSF MRI grant 2117445. Use of the Advanced Photon Source was supported by U.S. Department of Energy, Office of Basic Energy Sciences, under Contract No. DE-AC02-06CH11357. Part of the research described in this paper was performed at the Canadian Light Source, a national research facility of the University of Saskatchewan, which is supported by the Canada Foundation for Innovation (CFI), the Natural Sciences and Engineering Research Council (NSERC), the Canadian Institutes of Health Research (CIHR), the Government of Saskatchewan, and the University of Saskatchewan. Solid-state NMR measurements were supported by the U.S. Department of Energy, Office of Science, Basic Energy Sciences, Materials Science and Engineering Division. The Ames National Laboratory is operated for the U.S. DOE by Iowa State University under Contract No. DE-AC02-07CH11358. The authors would like to thank Prof. J. V. Zaikina (ISU) for access to the SPS and UV-Vis spectrometer; Dr W. Xu, for help with conducting in situ PXRD at beamline 17-BM at APS-ANL, and Dr A. Leontowich at the Canadian Light Source, BXDS beamline for help with collecting the highresolution PXRD used for Rietveld refinement.

# References

1 A. Banerjee, X. Wang, C. Fang, E. A. Wu and Y. S. Meng, Interfaces and Interphases in All-Solid-State Batteries with

- Inorganic Solid Electrolytes, Chem. Rev., 2020, 120(14), 6878-6933, DOI: 10.1021/acs.chemrev.0c00101.
- 2 F. Croce, G. B. Appetecchi, L. Persi and B. Scrosati, Nanocomposite Polymer Electrolytes for Lithium Batteries, Nature, 1998, 394(6692), 456-458, DOI: 10.1038/28818.
- 3 D. Zhou, D. Shanmukaraj, A. Tkacheva, M. Armand and G. Wang, Polymer Electrolytes for Lithium-Based Batteries: Advances and Prospects, Chem, 2019, 5(9), 2326–2352, DOI: 10.1016/j.chempr.2019.05.009.
- 4 X. Yao, B. Huang, J. Yin, G. Peng, Z. Huang, C. Gao, D. Liu and X. Xu, All-Solid-State Lithium Batteries with Inorganic Solid Electrolytes: Review of Fundamental Science, Chin. Phys. B, 2015, 25(1), 018802, DOI: 10.1088/1674-1056/25/1/ 018802.
- 5 M. Matsuo and S. Orimo, Lithium Fast-Ionic Conduction in Complex Hydrides: Review and Prospects, Adv. Energy Mater., 2011, 1(2), 161-172, DOI: 10.1002/aenm.201000012.
- 6 X. Li, J. Liang, N. Chen, J. Luo, K. R. Adair, C. Wang, M. N. Banis, T.-K. Sham, L. Zhang, S. Zhao, S. Lu, H. Huang, R. Li and X. Sun, Water-Mediated Synthesis of a Superionic Halide Solid Electrolyte, Angew. Chem., 2019, 131(46), 16579-16584, DOI: 10.1002/ange.201909805.
- 7 X. Li, J. Liang, J. Luo, M. N. Banis, C. Wang, W. Li, S. Deng, C. Yu, F. Zhao, Y. Hu, T.-K. Sham, L. Zhang, S. Zhao, S. Lu, H. Huang, R. Li, K. R. Adair and X. Sun, Air-Stable Li 3 InCl 6 Electrolyte with High Voltage Compatibility for All-Solid-State Batteries, Energy Environ. Sci., 2019, 12(9), 2665-2671, DOI: 10.1039/C9EE02311A.
- 8 M. Tatsumisago and A. Hayashi, Sulfide Glass-Ceramic Electrolytes for All-Solid-State Lithium and Sodium Batteries, Int. J. Appl. Glass Sci., 2014, 5(3), 226-235, DOI: 10.1111/ijag.12084.
- 9 Y. Kato, S. Hori, T. Saito, K. Suzuki, M. Hirayama, A. Mitsui, M. Yonemura, H. Iba and R. Kanno, High-Power All-Solid-State Batteries Using Sulfide Superionic Conductors, Nat. Energy, 2016, 1(4), 1-7, DOI: 10.1038/nenergy.2016.30.
- 10 Q. Zhao, S. Stalin, C.-Z. Zhao and L. A. Archer, Designing Solid-State Electrolytes for Safe, Energy-Dense Batteries, Nat. Rev. Mater., 2020, 5(3), 229-252, DOI: 10.1038/s41578-019-0165-5.
- 11 D. H. S. Tan, A. Banerjee, Z. Chen and Y. S. Meng, From Nanoscale Interface Characterization to Sustainable Energy Storage Using All-Solid-State Batteries, Nat. Nanotechnol., 2020, 15(3), 170-180, DOI: 10.1038/s41565-020-0657-x.
- 12 Z. Gao, H. Sun, L. Fu, F. Ye, Y. Zhang, W. Luo and Y. Huang, Promises, Challenges, and Recent Progress of Inorganic Solid-State Electrolytes for All-Solid-State Lithium Batteries, Adv. Mater., 2018, 30(17), 1705702, DOI: 10.1002/ adma.201705702.
- 13 R. Kanno and M. Murayama, Lithium Ionic Conductor Thio-LISICON: The Li<sub>2</sub>S-GeS<sub>2</sub>-P<sub>2</sub>S<sub>5</sub> System, J. Electrochem. Soc., 2001, 148(7), A742, DOI: 10.1149/1.1379028.
- 14 T. Famprikis, P. Canepa, J. A. Dawson, M. S. Islam and C. Masquelier, Fundamentals of Inorganic Solid-State Electrolytes for Batteries, Nat. Mater., 2019, 18(12), 1278-1291, DOI: 10.1038/s41563-019-0431-3.

- 15 A. Han, R. Tian, L. Fang, F. Wan, X. Hu, Z. Zhao, F. Tu, D. Song, X. Zhang and Y. Yang, A Low-Cost Liquid-Phase Method of Synthesizing High-Performance Li<sub>6</sub>PS<sub>5</sub>Cl Solid-Electrolyte, ACS Appl. Mater. Interfaces, 2022, 14(27), 30824-30838, DOI: 10.1021/acsami.2c06075.
- 16 S. Wang, Y. Zhang, X. Zhang, T. Liu, Y.-H. Lin, Y. Shen, L. Li and C.-W. Nan, High-Conductivity Argyrodite Li<sub>6</sub>PS<sub>5</sub>Cl Solid Electrolytes Prepared via Optimized Sintering Processes for All-Solid-State Lithium-Sulfur Batteries, ACS Appl. Mater. Interfaces, 2018, 10(49), 42279-42285, DOI: 10.1021/ acsami.8b15121.
- 17 M. R. Busche, D. A. Weber, Y. Schneider, C. Dietrich, S. Wenzel, T. Leichtweiss, D. Schröder, W. Zhang, H. Weigand, D. Walter, S. J. Sedlmaier, D. Houtarde, L. F. Nazar and J. Janek, In Situ Monitoring of Fast Li-Ion Conductor Li<sub>7</sub>P<sub>3</sub>S<sub>11</sub> Crystallization Inside a Hot-Press Setup, Chem. Mater., 2016, 28(17), 6152-6165, DOI: 10.1021/acs.chemmater.6b02163.
- 18 P. Bron, S. Dehnen and B. Roling,  $Li_{10}Si_{0.3}Sn_{0.7}P_2S_{12}$  A Low-Low-Grain-Boundary-Resistance Superionic Conductor, J. Power Sources, 2016, 329, 530-535, DOI: 10.1016/j.jpowsour.2016.08.115.
- 19 N. Kamaya, K. Homma, Y. Yamakawa, M. Hirayama, R. Kanno, M. Yonemura, T. Kamiyama, Y. Kato, S. Hama, K. Kawamoto and A. Mitsui, A Lithium Superionic Conductor, Nat. Mater., 2011, 10(9), 682-686, DOI: 10.1038/ nmat3066.
- 20 Y. Huang, B. Shao and F. Han, Interfacial Challenges in All-Solid-State Lithium Batteries, Curr. Opin. Electrochem., 2022, 33, 100933, DOI: 10.1016/j.coelec.2021.100933.
- 21 A. D. Sendek, E. R. Antoniuk, E. D. Cubuk, B. Ransom, B. E. Francisco, J. Buettner-Garrett, Y. Cui and E. J. Reed, Combining Superionic Conduction and Favorable Decomposition Products in the Crystalline Lithium-Boron-Sulfur System: A New Mechanism for Stabilizing Solid Li-Ion Electrolytes, ACS Appl. Mater. Interfaces, 2020, 12(34), 37957-37966, DOI: 10.1021/acsami.9b19091.
- 22 X. Zhu, Z. Zhang, L. Chen, H. Li and F. Wu, Progress in Lithium Thioborate Superionic Conductors, J. Mater. Res., 2022, 37(19), 3269-3282, DOI: 10.1557/s43578-022-00592-4.
- 23 F. Hiltmann, P. Zum Hebel, A. Hammerschmidt and B. Krebs, Li<sub>5</sub>B<sub>7</sub>S<sub>13</sub> und Li<sub>9</sub>B<sub>19</sub>S<sub>33</sub>: Zwei Lithiumthioborate mit neuen hochpolymeren Anionengerüsten, Z. Anorg. Allg. 293-302, DOI: Chem., 1993, 619(2), 10.1002/ zaac.19936190212.
- 24 K. Kaup, A. Assoud, J. Liu and L. F. Nazar, Fast Li-Ion Conductivity in Superadamantanoid Lithium Thioborate Halides, Angew. Chem., Int. Ed., 2021, 60(13), 6975-6980, DOI: 10.1002/anie.202013339.
- 25 K. Kaup, K. Bishop, A. Assoud, J. Liu and L. F. Nazar, Fast Ion-Conducting Thioboracite with a Perovskite Topology and Argyrodite-like Lithium Substructure, J. Am. Chem. Soc., 2021, 143(18), 6952-6961, DOI: 10.1021/jacs.1c00941.
- 26 Y. Ma, J. Wan, X. Xu, A. D. Sendek, S. E. Holmes, B. Ransom, Z. Jiang, P. Zhang, X. Xiao, W. Zhang, R. Xu, F. Liu, Y. Ye, E. Kaeli, E. J. Reed, W. C. Chueh and Y. Cui, Experimental Discovery of a Fast and Stable Lithium Thioborate Solid

- Electrolyte,  $\text{Li}_{6+2x}[B_{10}S_{18}]S_x$  (x  $\approx$  1), ACS Energy Lett., 2023, 8(6), 2762-2771, DOI: 10.1021/acsenergylett.3c00560.
- 27 J. Cho and S. W. Martin, Infrared Spectra of Lithium Thioborate Glasses and Polycrystals, J. Non-Cryst. Solids, 1994, 170(2), 182-189, DOI: 10.1016/0022-3093(94)90045-0.
- 28 A. E. Burns, M. Royle and S. W. Martin, Infrared Spectroscopy of AgI Doped Ag<sub>2</sub>S+B<sub>2</sub>S<sub>3</sub> Fast Ion Conducting Thioborate Glasses, J. Non-Cryst. Solids, 2000, 262(1), 252-257, DOI: 10.1016/S0022-3093(99)00652-3.
- 29 S.-J. Hwang, C. Fernandez, J. P. Amoureux, J. Cho, S. W. Martin and M. Pruski, Quantitative Study of the Short Range Order in B2O3 and B2S3 by MAS and Two-Dimensional Triple-Quantum MAS 11B NMR, Solid State Nucl. Magn. Reson., 1997, 8(2), 109-121, DOI: 10.1016/ S0926-2040(96)01280-5.
- 30 B. Curtis, C. Francis, S. Kmiec and S. W. Martin, Investigation of the Short Range Order Structures in Sodium Thioborosilicate Mixed Glass Former Glasses, J. Non-Cryst. Solids, 2019, 521, 119456, DOI: 10.1016/ j.jnoncrysol.2019.05.032.
- 31 S.-J. Hwang, C. Fernandez, J. P. Amoureux, J.-W. Han, J. Cho, S. W. Martin and M. Pruski, Structural Study of  $xNa_2S+(1-x)$ B<sub>2</sub>S<sub>3</sub> Glasses and Polycrystals by Multiple-Quantum MAS NMR of <sup>11</sup>B and <sup>23</sup>Na, J. Am. Chem. Soc., 1998, 120(29), 7337-7346, DOI: 10.1021/ja9800481.
- 32 S. W. Martin, R. Christensen, G. Olson, J. Kieffer and W. Wang, New Interpretation of Na<sup>+</sup>-Ion Conduction in and the Structures and Properties of Sodium Borosilicate Mixed Glass Former Glasses, J. Phys. Chem. C, 2019, 123(10), 5853-5870, DOI: 10.1021/acs.jpcc.8b11735.
- 33 L. Zhou, J. D. Bazak, B. Singh, C. Li, A. Assoud, N. M. Washton, V. Murugesan and L. F. Nazar, A New Sodium Thioborate Fast Ion Conductor: Na<sub>3</sub>B<sub>5</sub>S<sub>9</sub>, Angew. Chem., Int. Ed., e202300404, DOI: 10.1002/anie.202300404.
- 34 J. Waugh and E. Fedin, Determination of Hindered-Rotation Barriers in Solids, Phys. Solid State, 1963, 4(8), 1633-1636.
- 35 T. Kaib, S. Haddadpour, M. Kapitein, P. Bron, C. Schröder, H. Eckert, B. Roling and S. Dehnen, New Lithium Chalcogenidotetrelates, LiChT: Synthesis and Characterization of the Li<sup>+</sup>-Conducting Tetralithium Ortho-Sulfidostannate Li<sub>4</sub>SnS<sub>4</sub>, Chem. Mater., 2012, 24(11), 2211-2219, DOI: 10.1021/cm3011315.
- 36 S. Neuberger, N. Mathew, S. Clement Adediwura and J. S. Günne, auf der. Influence of Mg on the Li Ion Mobility in Li<sub>4-2x</sub>Mg<sub>x</sub>P<sub>2</sub>S<sub>6</sub>, Dalton Trans., 2023, 52(45), 16894-16902, DOI: 10.1039/D3DT02624H.
- 37 R. Bertermann, W. Müller-Warmuth, C. Jansen, F. Hiltmann and B. Krebs, NMR Studies of the Lithium Dynamics in Two Thioborate Superionic Conductors:  $Li_9B_{19}S_{33}$  $\text{Li}_{4-2x}\text{Sr}_{2+x}\text{B}_{10}\text{S}_{19}$  (x \approx 0.27), Solid State Ionics, 1999, 117(3), 245-255, DOI: 10.1016/S0167-2738(98)00407-X.
- 38 S. Muy, J. Voss, R. Schlem, R. Koerver, S. J. Sedlmaier, F. Maglia, P. Lamp, W. G. Zeier and Y. Shao-Horn, High-Throughput Screening of Solid-State Li-Ion Conductors Using Lattice-Dynamics Descriptors, iScience, 2019, 16, 270-282, DOI: 10.1016/j.isci.2019.05.036.

- 39 H. Park, S. Yu and D. J. Siegel, Predicting Charge Transfer Stability between Sulfide Solid Electrolytes and Li Metal Anodes, *ACS Energy Lett.*, 2021, **6**(1), 150–157, DOI: **10.1021/acsenergylett.0c02**372.
- 40 M. S. Diallo, T. Shi, Y. Zhang, X. Peng, I. Shozib, Y. Wang, L. J. Miara, M. C. Scott, Q. H. Tu and G. Ceder, Effect of Solid-Electrolyte Pellet Density on Failure of Solid-State Batteries, *Nat. Commun.*, 2024, 15(1), 858, DOI: 10.1038/ s41467-024-45030-7.
- 41 S. Muy, J. C. Bachman, H.-H. Chang, L. Giordano, F. Maglia, S. Lupart, P. Lamp, W. G. Zeier and Y. Shao-Horn, Lithium Conductivity and Meyer-Neldel Rule in Li<sub>3</sub>PO<sub>4</sub>–Li<sub>3</sub>VO<sub>4</sub>–Li<sub>4</sub>GeO<sub>4</sub> Lithium Superionic Conductors, *Chem. Mater.*, 2018, 30(16), 5573–5582, DOI: 10.1021/acs.chemmater.8b01504.
- 42 S. Harm, A.-K. Hatz, I. Moudrakovski, R. Eger, A. Kuhn, C. Hoch and B. V. Lotsch, Lesson Learned from NMR: Characterization and Ionic Conductivity of LGPS-like Li<sub>7</sub>SiPS<sub>8</sub>, Chem. Mater., 2019, 31(4), 1280–1288, DOI: 10.1021/acs.chemmater.8b04051.
- 43 S. W. Martin, H. J. Bischof, M. Mali, J. Roos and D. Brinkmann, 109Ag NMR Investigations of the

- Superionic Glasses  $(AgI)_x \cdot (Ag_2O \cdot 2B_2O_3)_{1-x}$ , Solid State Ionics, 1986, **18–19**, 421–425, DOI: **10.1016/0167-2738(86) 90153-0**.
- 44 F. Borsa, D. R. Torgeson, S. W. Martin and H. K. Patel, Relaxation and Fluctuations in Glassy Fast-Ion Conductors: Wide-Frequency-Range NMR and Conductivity Measurements, *Phys. Rev. B:Condens. Matter Mater. Phys.*, 1992, **46**(2), 795–800, DOI: **10.1103/PhysRevB.46.795**.
- 45 I. Svare, F. Borsa, D. R. Torgeson and S. W. Martin, Correlation Functions for Ionic Motion from NMR Relaxation and Electrical Conductivity in the Glassy Fast-Ion Conductor (Li<sub>2</sub>S)<sub>0.56</sub>(SiS<sub>2</sub>)<sub>0.44</sub>, *Phys. Rev. B:Condens. Matter Mater. Phys.*, 1993, 48(13), 9336–9344, DOI: 10.1103/ PhysRevB.48.9336.
- 46 C. Mi and S. R. Hall, Preparation and Degradation of High Air Stability Sulfide Solid Electrolyte 75Li<sub>2</sub>S·25P<sub>2</sub>S<sub>5</sub> Glass-Ceramic, *Solid State Ionics*, 2023, **389**, 116106, DOI: **10.1016/j.ssi.2022.116106**.
- 47 CCDC 2475362: Experimental Crystal Structure Determination, 2025, DOI: 10.5517/ccdc.csd.cc2p2td0.